# A TIRE CONTACT SOLUTION TECHNIQUE

John T. Tielking
Civil Engineering Department
Texas A&M University

## EXPANDED ABSTRACT

An efficient method for calculating the contact boundary and interfacial pressure distribution has been developed. This solution technique utilizes the discrete Fourier transform to establish an influence coefficient matrix for the portion of the pressurized tire surface that may be in the contact region. This matrix is used in a linear algebra algorithm to determine the contact boundary and the array of forces within the boundary that are necessary to hold the tire in equilibrium against a specified contact surface. The algorithm also determines the normal and tangential displacements of those points on the tire surface that are included in the influence coefficient matrix. Displacements within and outside the contact region are calculated.

The solution technique is implemented here with a finite-element tire model that is based on orthotropic, nonlinear shell of revolution elements which can respond to nonaxisymmetric loads (refs. 1, 2). The basic characteristics of this relatively comprehensive tire model are described in reference 3. This presentation will focus on the contact solution technique published in reference 4. A sample contact solution is presented for the 32 × 8.8 Type VII aircraft tire that was studied in reference 5.

# FINITE-ELEMENT TIRE MODEL

The tire is modeled by an assemblage of axisymmetric curved shell elements. The elements are connected to form a meridian of arbitrary curvature and are located at the carcass midsurface. Figure 1 shows the assembly of 21 elements along the midsurface of a G78-14 tire, for which calculated results are shown in this paper. A cylindrical coordinate system is used, with r, θ, and z indicating the radial, circumferential, and axial directions, respectively. Each element forms a complete ring which is initially axisymmetric with respect to z. The elements are connected at nodal circles, hereafter referred to as nodes.

The finite elements are homogeneous orthotropic with a set of moduli specified for each individual element. The orthotropic moduli for each element are determined by the ply structure surrounding the element. Each ply (on each element) is specified separately, thereby allowing the model to include carcass details such as an overhead belt, sidewall reinforcement, and turnups. A turnup is included in the G78-14 tire model. It was found necessary to include the turnup in the model to obtain the correct inflated shape.
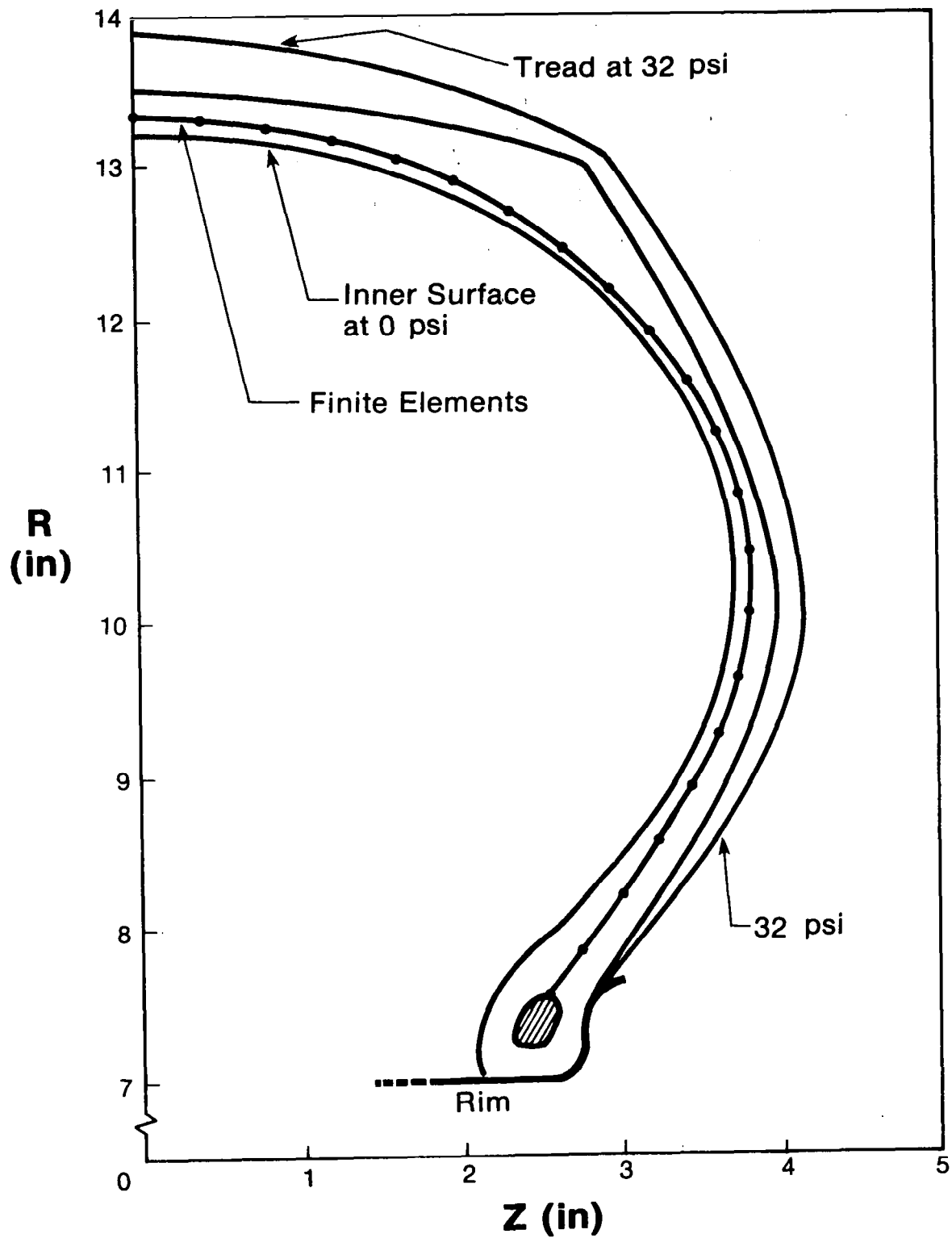
Figure 1

## SINGLE HARMONIC RING LOADS

The finite element tire model will respond to single harmonic ring loads on the nodal circles. An approximately linear load-deflection response is obtained when an individual ring load is applied to any node of the pressurized tire model. An example ring load-deflection calculation for the G78-14 tire model is shown in figure 2. A harmonic sequence of stiffness matrices is obtained by applying a sequence of single harmonic ring loads to each of the nodes that may be in the tire-pavement contact region.
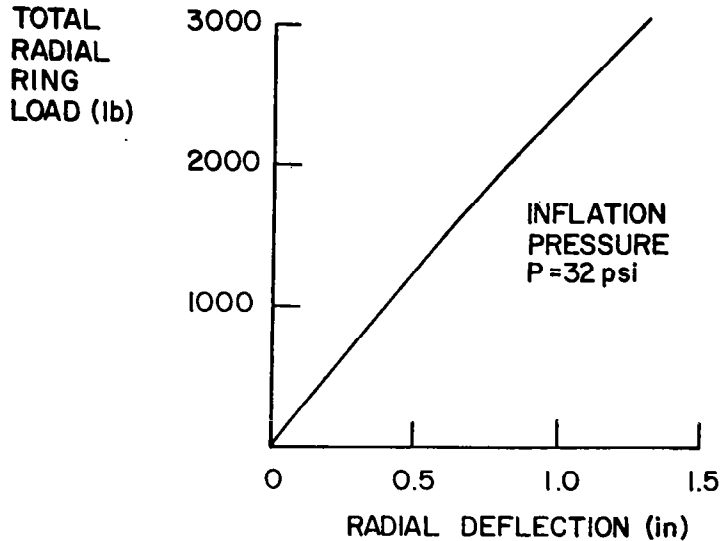


CROWN LOAD-DEFLECTION DATA CALCULATED WITH A UNIFORM RING LOAD APPLIED TO THE CROWN NODE
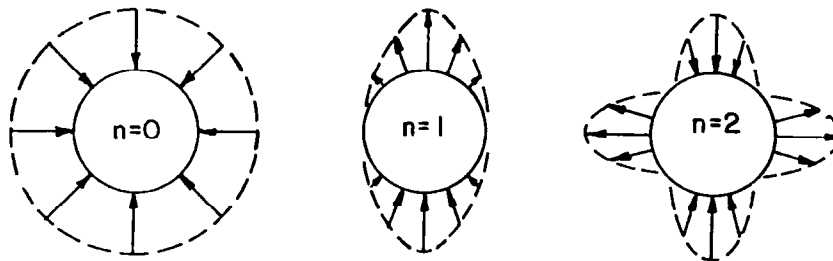


SINGLE HARMONIC RING LOADS APPLIED TO A FINITE ELEMENT NODE

Figure 2

## TRANSFER-FUNCTION DEFINITION

As a consequence of the linearity of the ring load-deflection response, the application of a single harmonic ring load produces a displacement field that varies circumferentially in the same harmonic as the applied ring load. Figure 3 gives the definition of the transfer function $T_n$ as the ratio of the output and input amplitudes. Since each node responds differently, a transfer-function matrix, $T_{ik|n}$, is needed to store the stiffness information generated by the ring loads.

INPUT:  Single Harmonic Ring Load    $A_n \cos n\theta$

OUTPUT:  Single Harmonic Displacement  $B_n \cos n\theta$

$$\text{TRANSFER FUNCTION} \quad T_n = \frac{B_n}{A_n}$$

$T_{ik|n}$ = $n^{th}$ harmonic transfer function relating displacement of node i to an $n^{th}$ harmonic ring load on node k

Figure 3

POINT LOAD VECTOR {p} AND THE DISCRETE FOURIER TRANSFORM (DFT)

This application of the discrete Fourier transform uses an even number of points (N), equally spaced around the circumference. The example shown in figure 4 uses N = 8 points. A unit load is applied at any point, say point 0. The DFT of the load vector yields a set of N coefficients, $G_j$, which are approximate values of the coefficients of the conventional Fourier series defined on the continuous interval $0 \leq \theta \leq 2\pi$ and representing the unit point load. The point load is applied, sequentially, in the radial, axial, and circumferential directions.

## INFLUENCE COEFFICIENT GENERATION
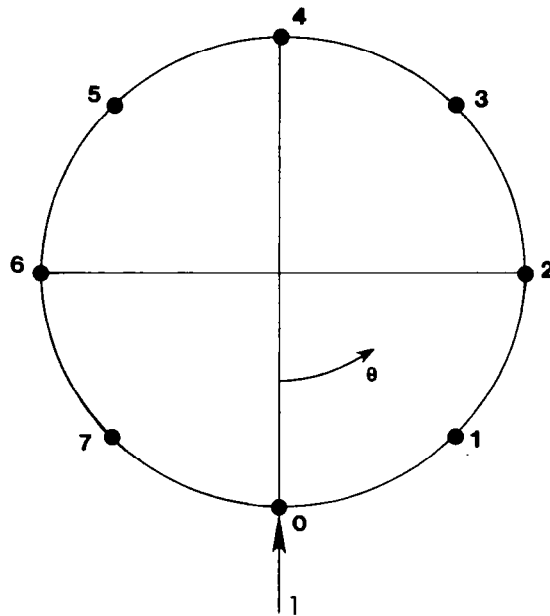


$$\{p\} = \{1, 0, 0, 0, 0, 0, 0, 0\} \quad \text{load vector}$$

$$\text{DFT} \quad G_j = \frac{1}{N} \sum_{k=0}^{N-1} g_k W_e^{jk} \qquad W_e = e^{-i2\pi/N}$$

$$g_k = \{p\}, \quad G_j = \frac{1}{N} \qquad j = 0, 1, \ldots, N-1$$

Figure 4

## INVERSE DISCRETE FOURIER TRANSFORM (IDFT) AND THE INFLUENCE COEFFICIENTS

Having the unit point load represented by a conventional Fourier series, whose coefficients $a_n$ are approximately given by the DFT coefficients, the transfer functions $T_{ik|n}$ are used, on each harmonic, to obtain the coefficients $b_n$ of the Fourier series representing the response of the nodal circle to the unit point load. The inverse discrete Fourier transform is then used to evaluate the displacements, $u_m$, at the N points. These displacements are the elements of the influence coefficient matrix $[A_{ijk\ell}]$ as seen in figure 5.

INPUT SERIES COEFFICIENTS $\quad a_n \approx G_n = \dfrac{1}{N}$

OUTPUT SERIES COEFFICIENTS $\quad b_n = a_n T_{ik|n} = \dfrac{1}{N} T_{ik|n}$

DFT OF DISPLACEMENT VECTOR $\quad G_n \approx b_n$

IDFT $\quad u_m^{ik} = \sum_{n=0}^{N-1} G_n W_e^{-mn} \qquad m = 0, 1, \ldots, N-1$

INFLUENCE COEFFICIENTS $\quad A_{ijk1} = u_{j-1}^{ik} \quad j = 1, 2, \ldots, N$

SHIFT: $\quad A_{ijk\ell} = u_{j-\ell}^{ik} \quad j = \ell, \ell+1, \ldots, N$

SYMMETRY: $\quad A_{k\ell ij} = A_{ijk\ell}$

$$\{d_{ij}\} = [A_{ijk\ell}]\{P_{k\ell}\}$$

Figure 5

# INFLUENCE COEFFICIENT MATRIX

The influence coefficient matrix relates the radial, axial, and circumferential components of the displacement of points on the tire surface to the radial, axial, and circumferential components of load at these points. The radial response partition shown in figure 6 is used to obtain a solution for frictionless contact, in which the axial and circumferential force components are known to be zero. The matrix here covers 3 points on each of 5 nodes. The point separation with this matrix is 11.25 degrees.

$P_{k\ell}$ = load at point $\ell$ on node k

$d_{ij}$ = deflection of point j on node i

$$\{d_{ij}\} = [A_{ijk\ell}] \{P_{k\ell}\}$$

$$
\begin{Bmatrix} d_{11} \\ d_{21} \\ d_{31} \\ d_{41} \\ d_{51} \\ d_{12} \\ d_{22} \\ d_{32} \\ d_{42} \\ d_{52} \end{Bmatrix}
=
\begin{bmatrix}
A_{1111} \\
A_{2111} & A_{2121} \\
A_{3111} & A_{3121} & A_{3131} \\
A_{4111} & A_{4121} & A_{4131} & A_{4141} \\
A_{5111} & A_{5121} & A_{5131} & A_{5141} & A_{5151} \\
A_{1211} & A_{1221} & A_{1231} & A_{1241} & A_{1251} & A_{1212} \\
A_{2211} & A_{2221} & A_{2231} & A_{2241} & A_{2251} & A_{2212} & A_{2222} \\
A_{3211} & A_{3221} & A_{3231} & A_{3241} & A_{3251} & A_{3212} & A_{3222} & A_{3232} \\
A_{4211} & A_{4221} & A_{4231} & A_{4241} & A_{4251} & A_{4212} & A_{4222} & A_{4232} & A_{4242} \\
A_{5211} & A_{5221} & A_{5231} & A_{5241} & A_{5251} & A_{5252} & A_{5222} & A_{5232} & A_{5242} & A_{5252}
\end{bmatrix}
\begin{Bmatrix} P_{11} \\ P_{21} \\ P_{31} \\ P_{41} \\ P_{51} \\ P_{12} \\ P_{22} \\ P_{32} \\ P_{42} \\ P_{52} \end{Bmatrix}
$$

Figure 6

## TOROIDAL SHELL CONTACT SCHEMATIC

After the inflation solution has been obtained, the tire model is deflected against a frictionless, flat surface. The contact surface is perpendicular to the wheel plane of symmetry and located at the specified loaded radius $R_\ell$, as shown in figure 7. The vertical load and the contact boundary are unknown a priori.



Figure 7

## RADIAL DEFLECTIONS IN THE CONTACT REGION

When the radius $R_\ell$ is specified, the radial deflections are given approximately by $r_{ij} = R_i \cos[(j-1)\Delta\theta] - R_\ell$, where $R_i$ is the inflation radius of node i and $\Delta\theta = 2\pi/N$ is the point spacing. Since the contact half-angle is usually less than 20°, the error in approximating the radial deflections by the above equation is not large. An initial estimate of the contact boundary is taken as the geometric intersection of the tire model and the contact surface. (See fig. 8.)



Figure 8

# LINE LOAD VECTORS

The radial deflections within the contact boundary are known but the forces that produce these deflections are unknown. The tangential (axial and circumferential) deflections within the contact boundary are unknown but the tangential forces are zero because the contact is frictionless. All surface forces are zero outside of the contact boundary. Since the number of unknowns (deflections and loads) is less than or equal to the number of equations established by the influence coefficient matrix, an initial contact solution can be found. The contact boundary is then adjusted to exclude negative radial forces. Three to five boundary adjustments are normally needed to converge on the contact solution. Figure 9 shows the load vectors obtained in a solution for the G78-14 tire with 221 kPa (32 psi) inflation pressure. The elements of {p} are values of the line load at 32 points on the tire model equator. The other vectors give line load values in the right (and left) half of the contact region. Seven nodal circles are in the contact region in this example.

**N:32**
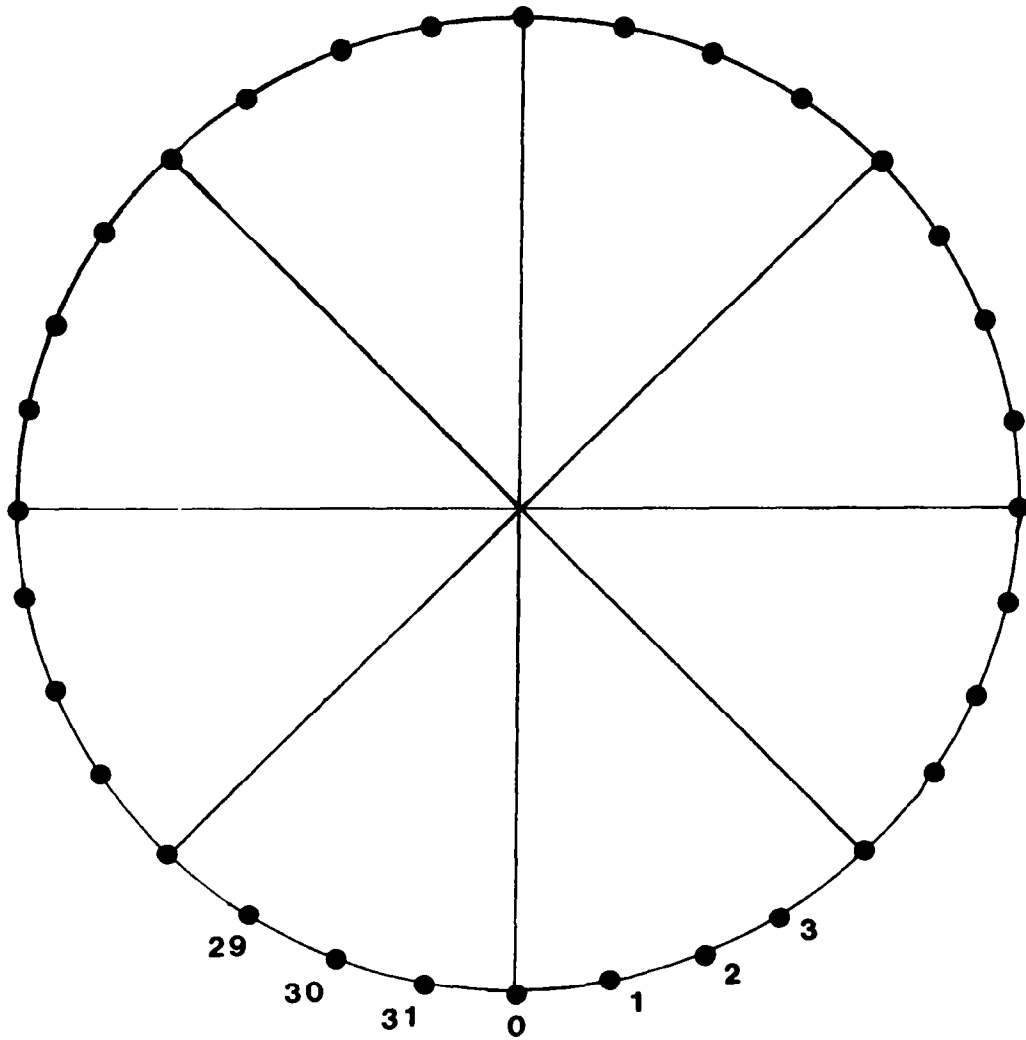


$$\{p^1\} = \{11.48, \ 5.67, \ 0, \ \ldots, \ 0, \ 5.67\} \quad lb/in$$

$$\{p^2\} = \{16.27, \ 4.61, \ 0, \ \ldots, \ 0, \ 4.61\}$$

$$\{p^3\} = \{22.28, \ 0, \ \ldots, \ 0\}$$

$$\{p^4\} = \{13.78, \ 0, \ \ldots, \ 0\}$$

Figure 9

## CONTACTING MERIDIAN AND EQUATOR

The line load values shown in figure 9 are divided by the point spacing to obtain the contact pressure at each point in the contact region. Figure 10 gives the contact pressure values at points on the meridian passing through the center of the contact region and at the three contacting points on the equator of the G78-14 tire. The tire surface points before contact are indicated by • and the same points after contact are indicated by ⊙ .
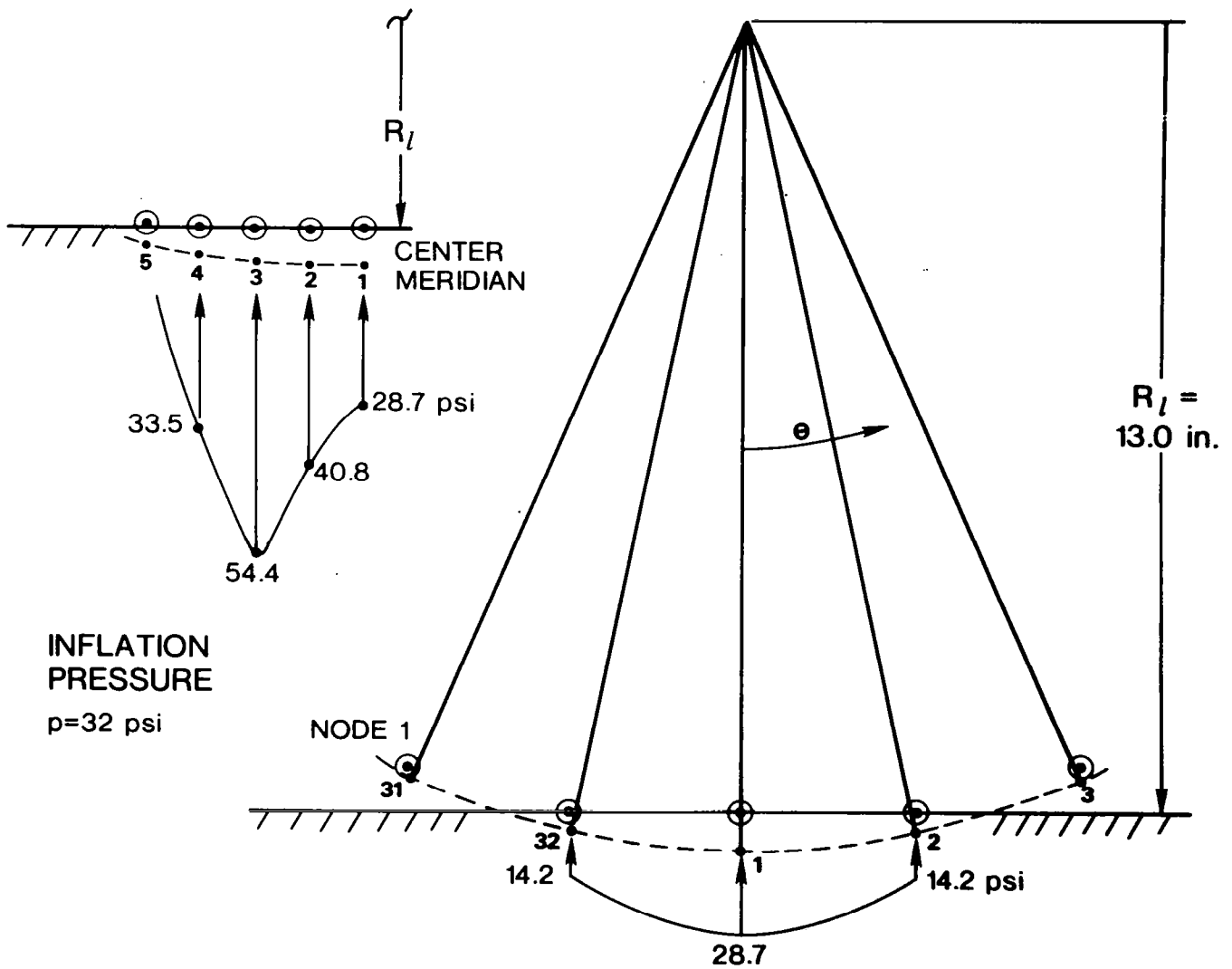


Figure 10

## CONTACT PRESSURE DISTRIBUTION

All of the contact pressure values (psi) calculated for the G78-14 tire with 221 kPa (32psi) inflation pressure are shown in figure 11. The estimated location of the contact boundary is shown as a dashed oval. The contact boundary will be more accurately located when the density of points covered by the influence coefficient matrix is increased. The point density is limited only by the size and speed of the computer used to execute the tire model program.

```
                    3.350E+01

                    5.439E+01

    1.143E+01       4.077E+01       1.143E+01

    1.424E+01       2.868E+01       1.424E+01

    1.143E+01       4.077E+01       1.143E+01

                    5.439E+01

                    3.350E+01
```

**CONTACT BOUNDARY**
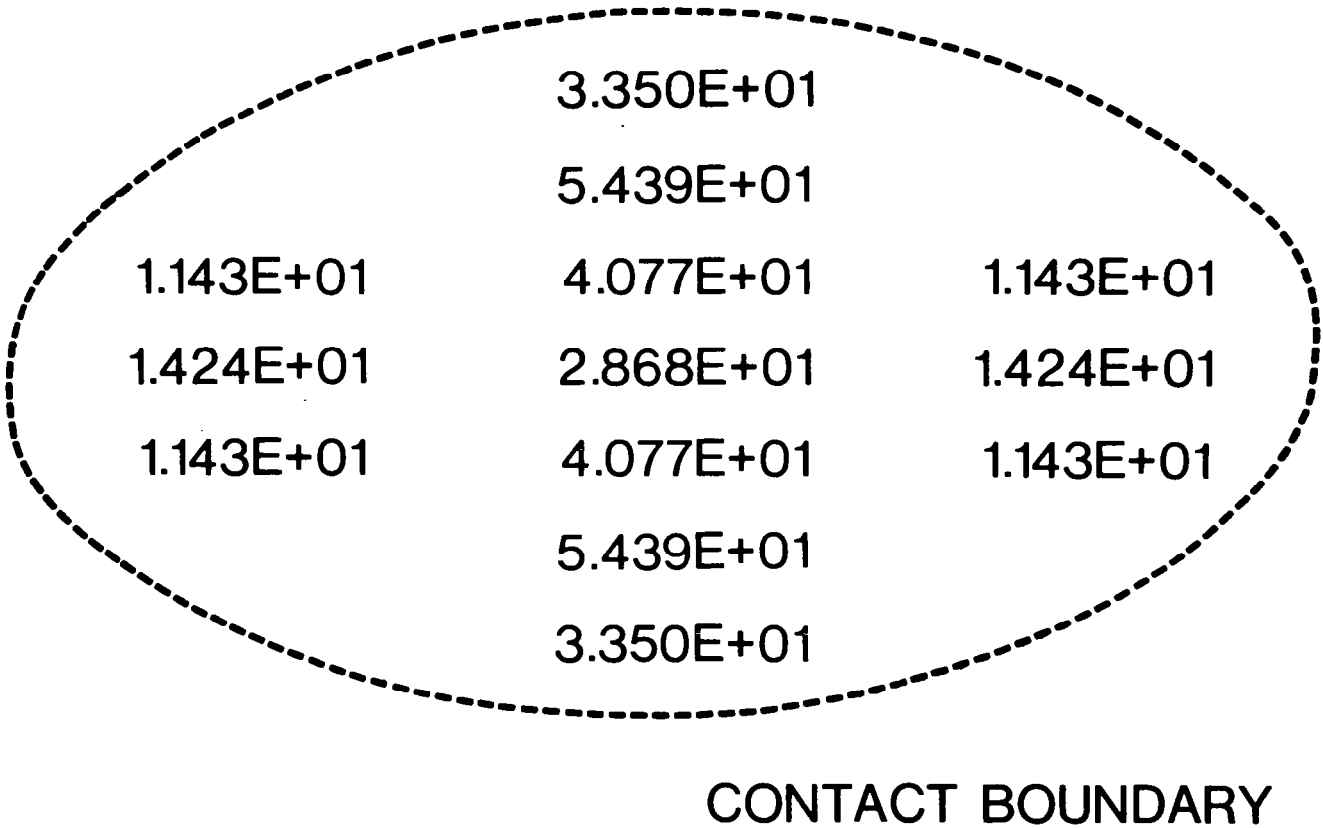
Figure 11

## AIRCRAFT TIRE SECTION

The remainder of this presentation shows the contact solution calculated for a 32 × 8.8 Type VII aircraft tire. A theoretical and experimental study of this tire under inflation pressure loading was made by Brewer (ref. 5). The photograph in figure 12 and the tire data shown in figure 13 are taken from reference 5. The white curve drawn on the tire section below marks the location of the carcass mid-surface.
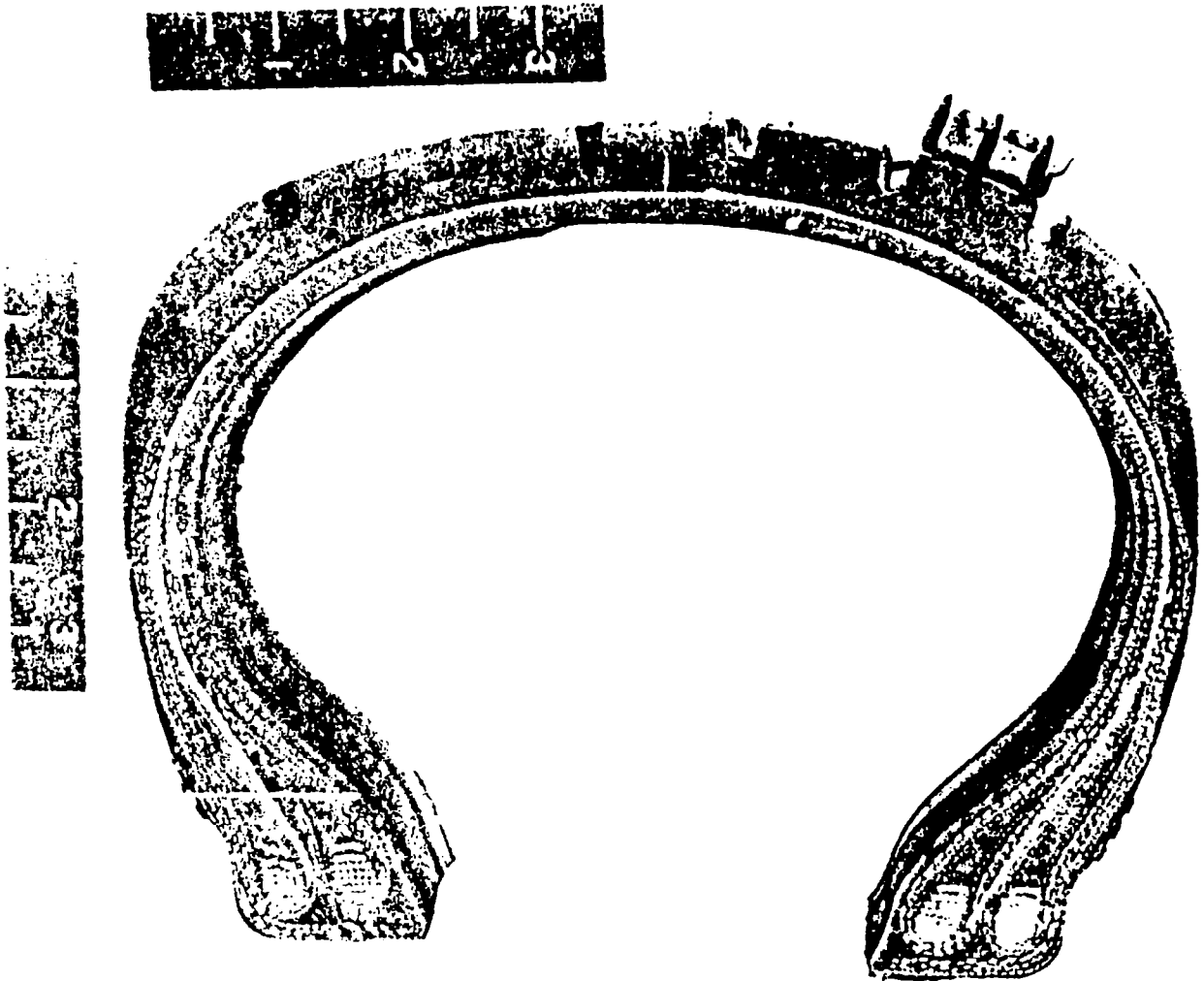


## MERIDIAN SECTION OF 32 X 8.8 AIRCRAFT TIRE

Figure 12

The parameters shown in figure 13 are used in a preprocessing subroutine to calculate homogeneous orthotropic properties for the finite element tire model.

# 32 x 8.8 TYPE VII
# AIRCRAFT TIRE

### Material Properties and Carcass Geometry

Rubber: $E_R$ = 450 psi, $\nu_R$ = 0.49, $G_R$ = 151 psi

Nylon Cord: $E_C$ = 156,000 psi, $\nu_C$ = 0.70, $G_C$ = 700 psi

Cord Diameter: $d_C$ = 0.031 in.

Ply Thickness: h = 0.043 in. (all plies)

### Cord Angle β (measured from meridian) and Cord Density N, by Lift Formula

| Element | β(deg) | N(epi) | Element | β(deg) | N(epi) |
|---------|--------|--------|---------|--------|--------|
| 1 | 55.44 | 25.42 | 12 | 46.97 | 23.81 |
| 2 | 55.35 | 25.39 | 13 | 45.34 | 23.75 |
| 3 | 55.20 | 25.34 | 14 | 43.71 | 23.78 |
| 4 | 54.96 | 25.26 | 15 | 41.99 | 23.88 |
| 5 | 54.60 | 25.15 | 16 | 40.25 | 24.08 |
| 6 | 54.08 | 25.00 | 17 | 38.64 | 24.35 |
| 7 | 53.33 | 24.79 | 18 | 37.13 | 24.68 |
| 8 | 52.34 | 24.55 | 19 | 35.73 | 25.05 |
| 9 | 51.18 | 24.32 | 20 | 34.39 | 25.48 |
| 10 | 49.90 | 24.10 | 21 | 33.37 | 25.85 |
| 11 | 48.49 | 23.93 | | | |

Construction: 6-ply, double bead

Figure 13

# FINITE ELEMENTS ON THE CARCASS MIDSURFACE

The aircraft tire is modeled with 21 finite elements positioned along the carcass midsurface. The ply structure in each element is specified separately in determining the homogeneous moduli for each element. Node 22 is a fixed node, positioned to represent the tire bead which does not displace or rotate. (See fig. 14.)
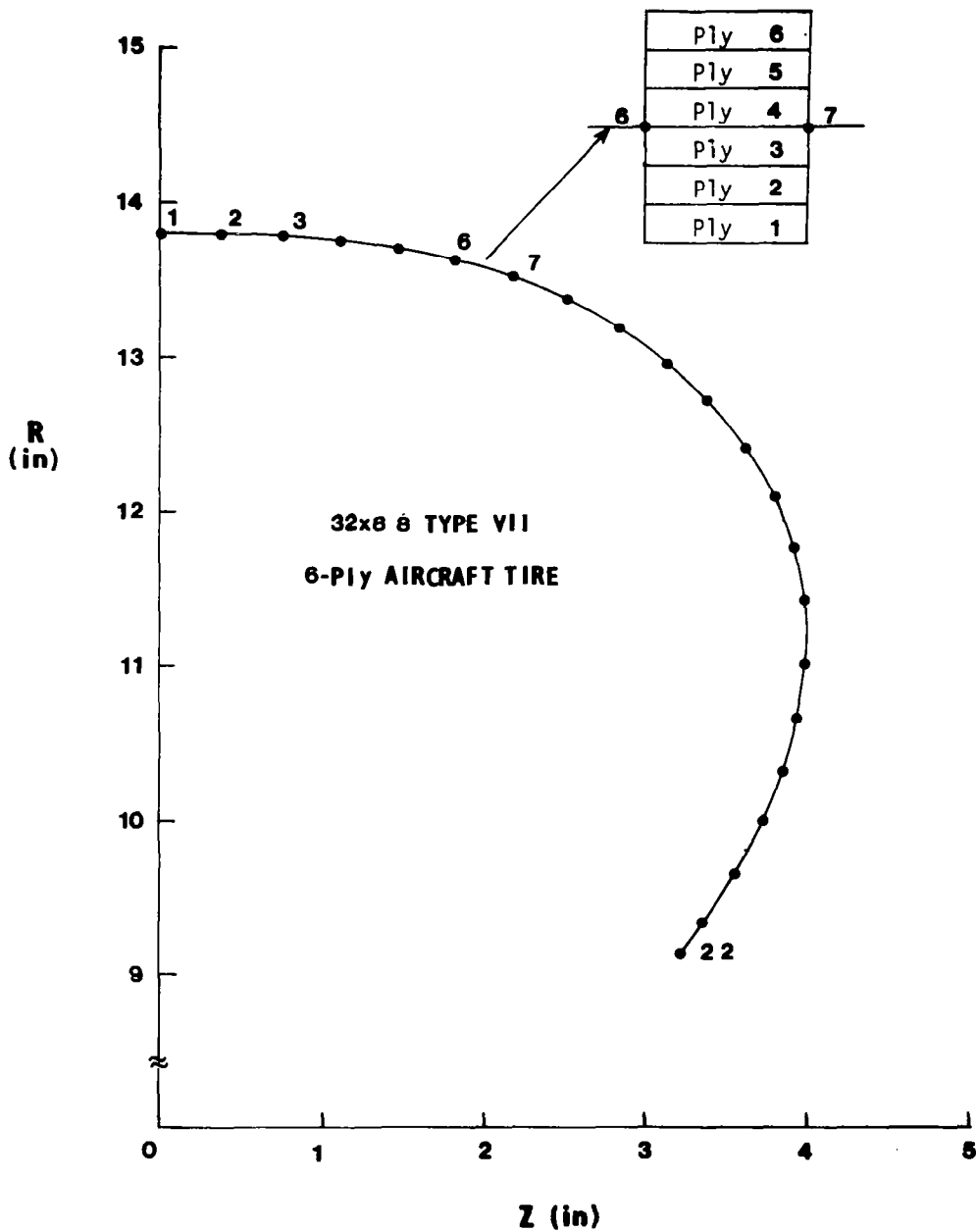


Figure 14

# LOAD VECTOR CORRECTION DATA

The problem of calculating tire shape due to inflation pressure is highly nonlinear. As recognized by Stafford and Tabaddor (ref 6.), a successful solution can only be obtained by a nonlinear finite element analysis which includes updating the pressure load vector direction during the inflation solution procedure. Table 1-1, in figure 15, gives the input load vector components, $p_n$ and $p_s$, that are needed in order to have the resultant pressure load normal to the inflated tire model.
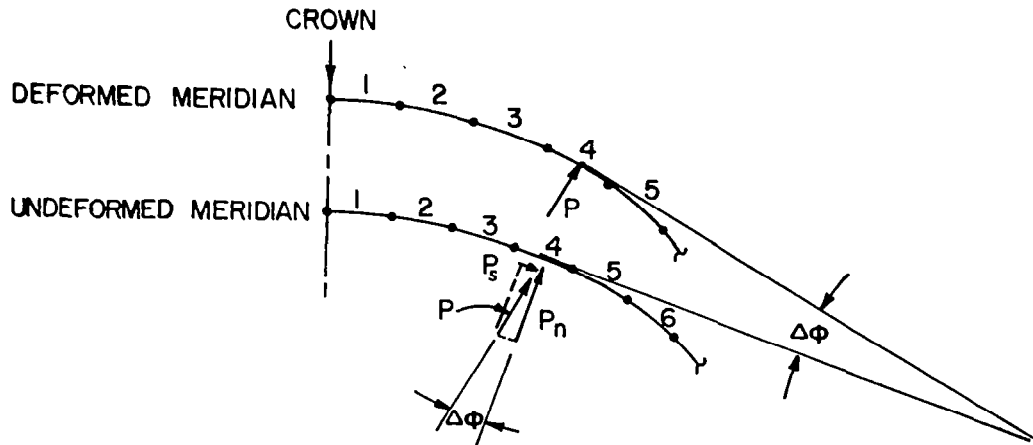


TABLE 1-1. INPUT LOAD DATA FOR FINITE ELEMENT MODEL OF AIRCRAFT TIRE ANALYZED BY BREWER

| Element Number | Rotation $\Delta\phi$ (deg) | TIRELOAD Input Pressure(psi) | |
| --- | --- | --- | --- |
| | | $P_n$ | $P_s$ |
| 1 | 1.46 | 94.97 | 2.41 |
| 2 | 4.61 | 94.69 | 7.63 |
| 3 | 7.68 | 94.15 | 12.70 |
| 4 | 10.10 | 93.53 | 16.64 |
| 5 | 11.23 | 93.17 | 18.55 |
| 6 | 10.71 | 93.35 | 17.65 |
| 7 | 9.19 | 93.78 | 15.17 |
| 8 | 7.90 | 94.09 | 13.11 |
| 9 | 7.18 | 94.26 | 11.87 |
| 10 | 6.48 | 94.39 | 10.71 |
| 11 | 5.39 | 94.58 | 8.92 |
| 12 | 3.00 | 94.87 | 4.97 |
| 13 | 2.24 | 94.93 | 3.70 |
| 14 | 0 | 95.00 | 0 |
| . | . | . | . |
| . | . | . | . |
| . | . | . | . |
| 21 | 0 | 95.00 | 0 |

Figure 15

# CROWN DISPLACEMENT VERSUS INFLATION PRESSURE

The effect of correcting the load vector is clearly seen in figure 16. The finite element solution obtained when the pressure direction remains normal to the undeformed elements is indicated by Δ's. The solution found when the pressure is normal to the deformed elements is indicated by ×'s. This solution compares well with the calculation and measurements made by Brewer (ref. 5).
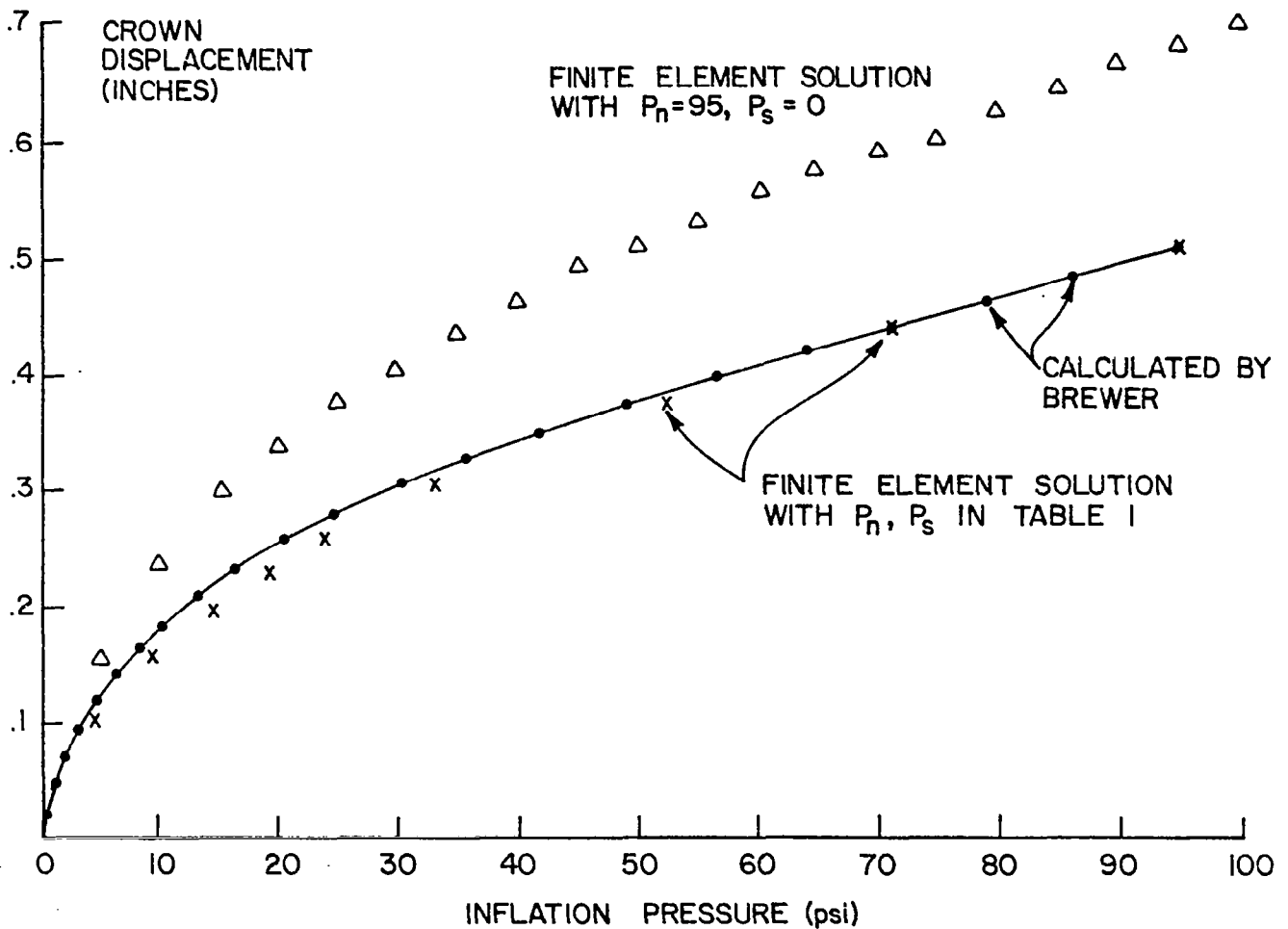


Figure 16

# DEFLECTED MERIDIAN

The deflected shape of the meridian passing through the center of contact is shown in figure 17 for the deflection $\delta$ = 19 mm (0.75 in.). The tire load calculated for this deflection is $F_y$ = 9.76 kN (2194 lb). The distribution of contact pressure along the meridian is also shown.
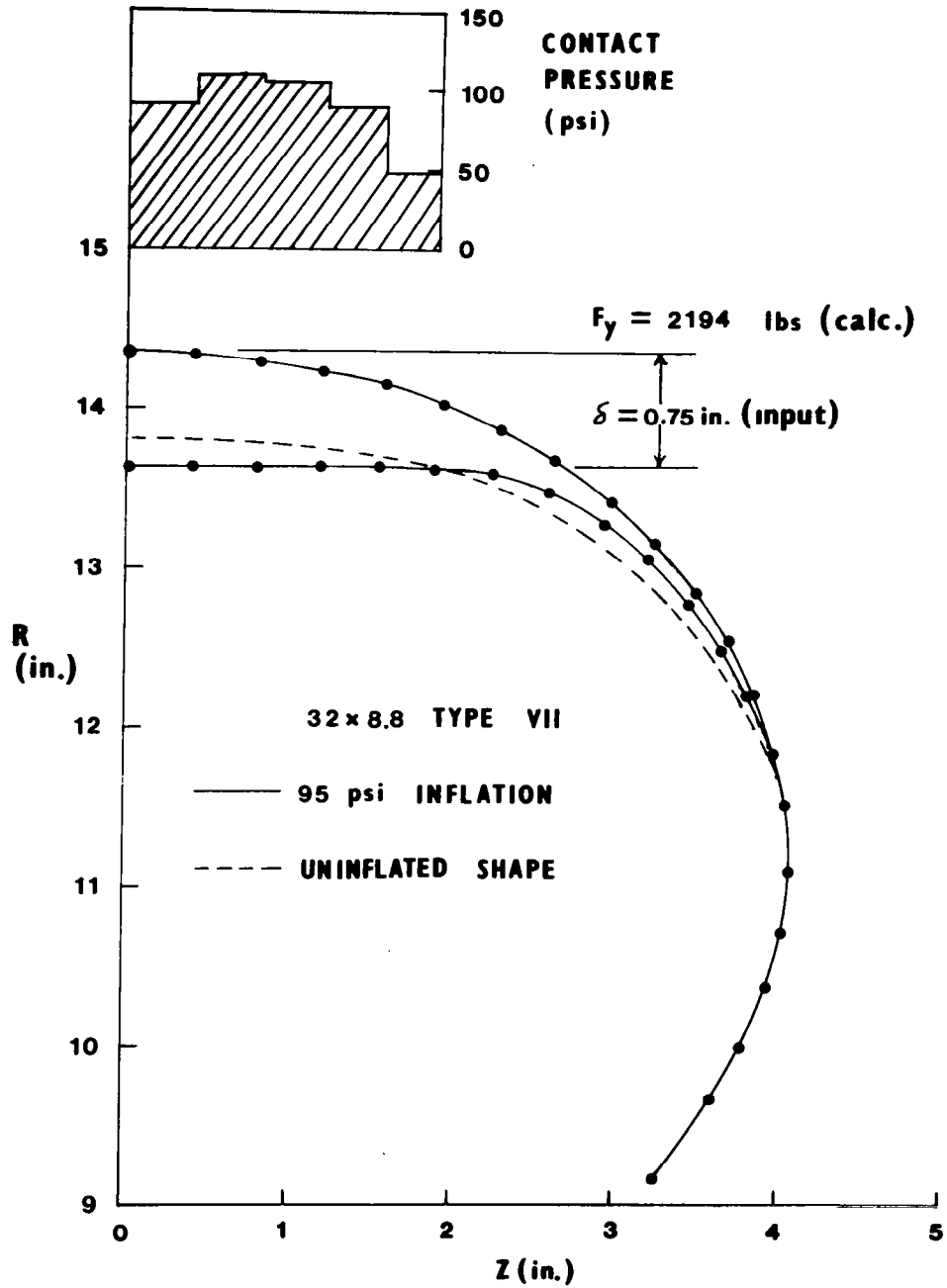


Figure 17

# DEFLECTED EQUATOR

The deflected shape of the equator and the distribution of contact pressure along it are shown in figure 18. Since only three points on the equator lie in the contact region, only a rough estimate of the circumferential location of the contact boundary can be made.



Figure 18

Calculated values of tire load for specified tire deflections are shown in figure 19.
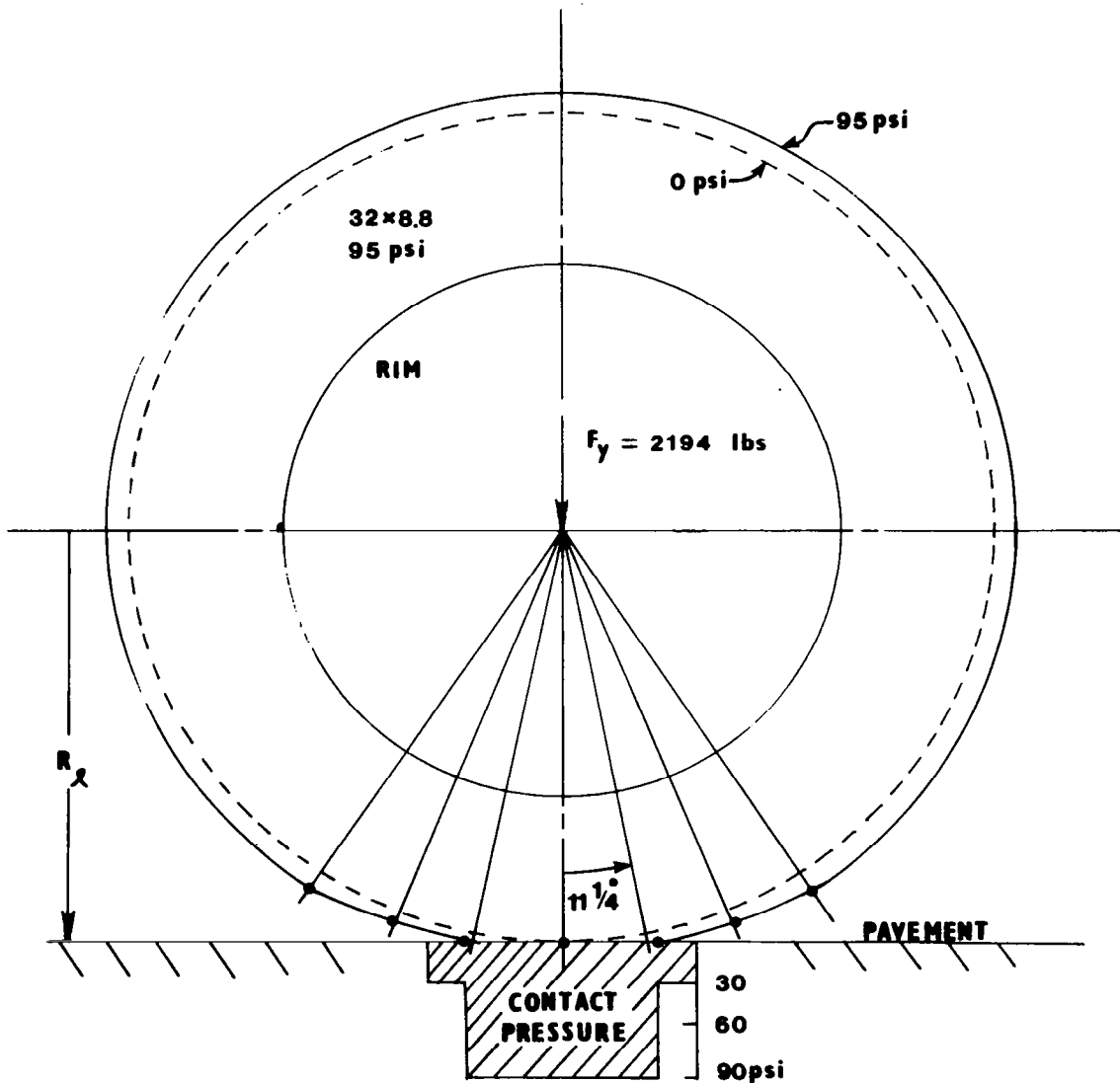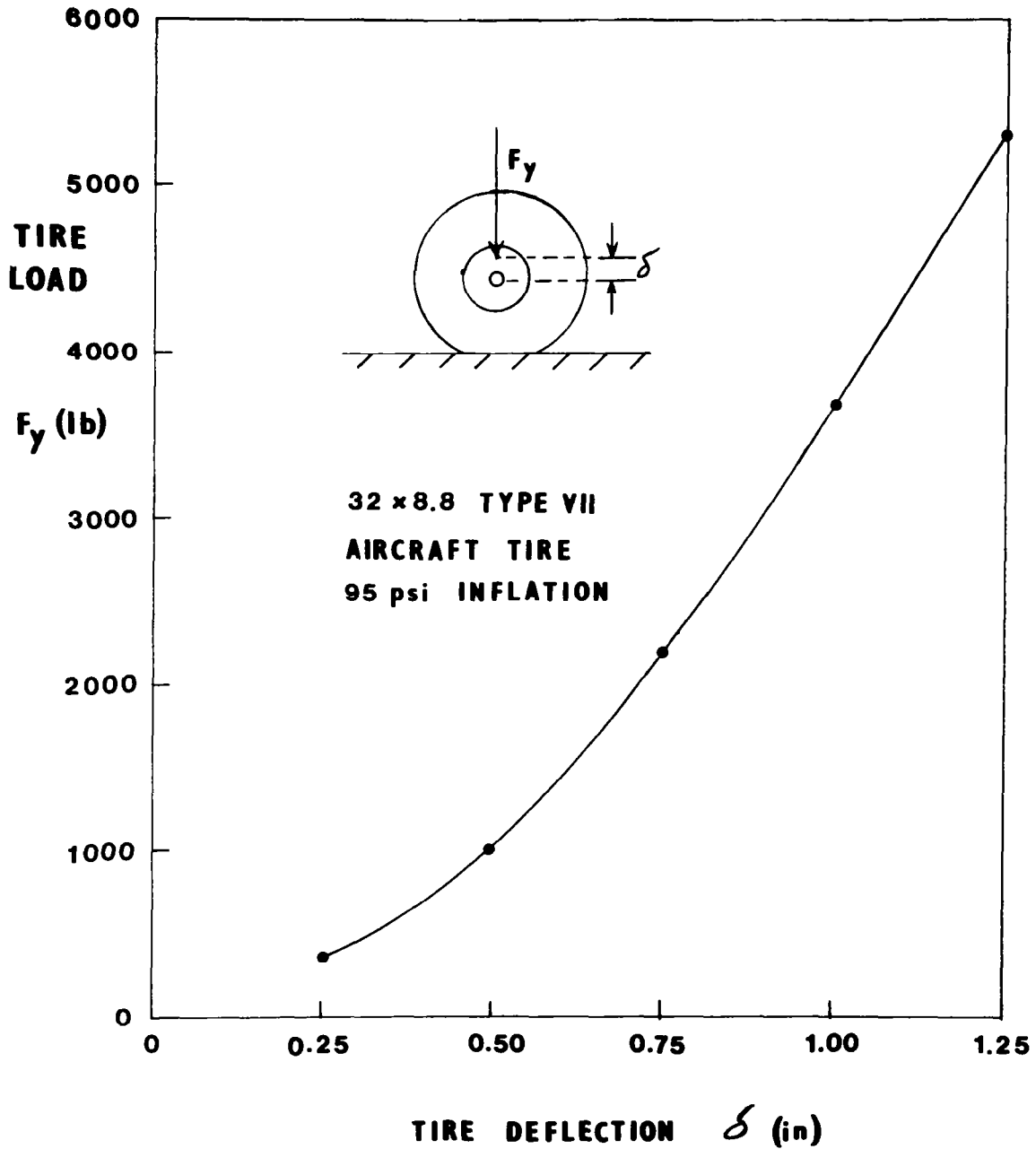


Figure 19

## CONTACT AREA VERSUS TIRE DEFLECTION

Calculated values of contact area for specified tire deflections are shown in figure 20. The calculated contact area increases in finite increments as additional points enter the contact region (as the load is increased).
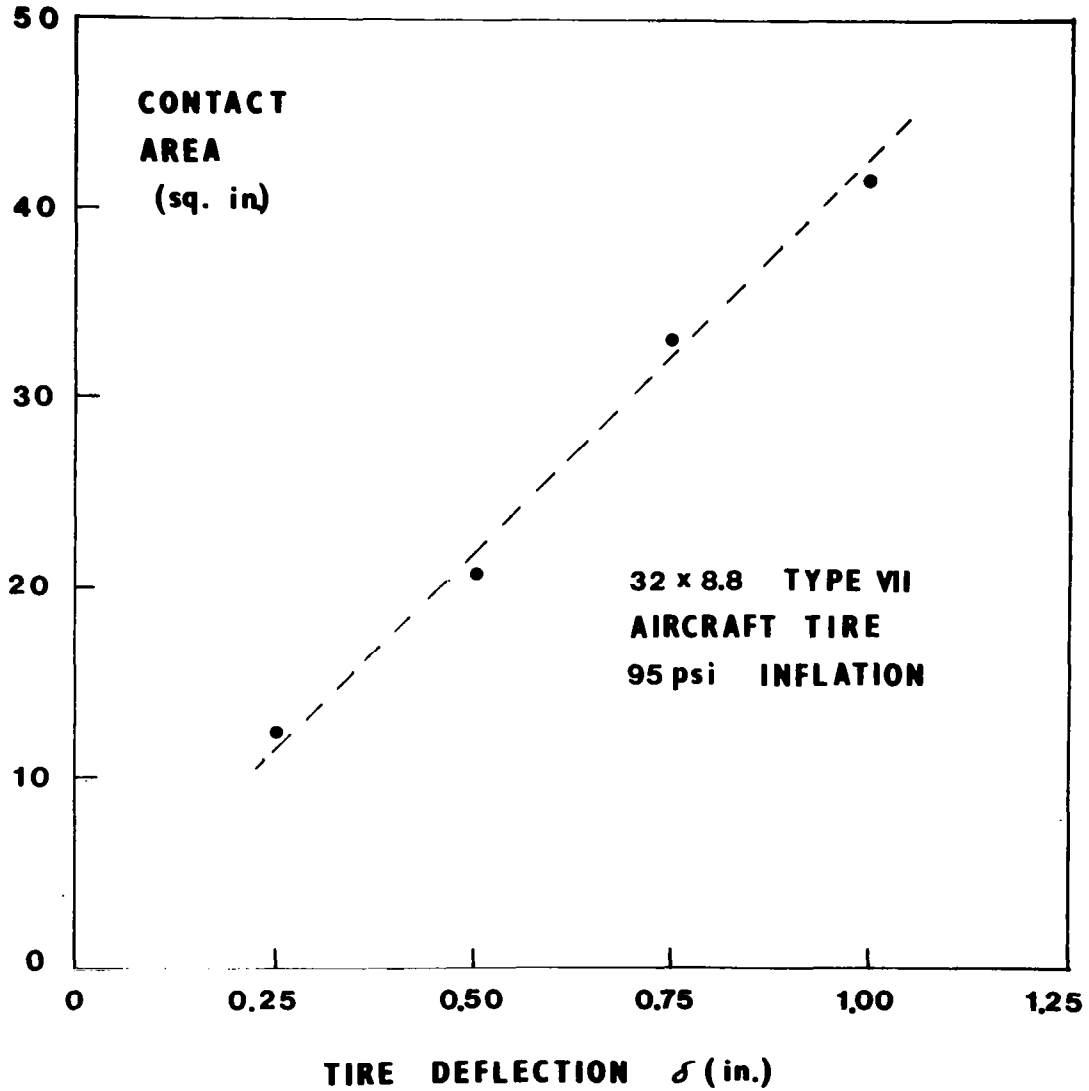


Figure 20

# CALCULATED CONTACT PRESSURE DISTRIBUTIONS

All of the contact pressure values (psi) calculated for two different tire loads are shown in figure 21. The tire inflation pressure is 655 kPa (95 psi).

## AIRCRAFT TIRE CONTACT PRESSURE DISTRIBUTIONS

|       |          |       |
|-------|----------|-------|
|       | 48.7     |       |
|       | 90.5     |       |
| 21.3  | 105.6    | 21.3  |
| 34.4  | 108.6    | 34.4  |
| 28.3  | 90.7 psi | 28.3  |
| 34.4  | 108.6    | 34.4  |
| 21.3  | 105.6    | 21.3  |
|       | 90.5     |       |
|       | 48.7     |       |

(a) δ = 0.75 in., Fz = 2200 lb

|       |           |       |
|-------|-----------|-------|
| 12.9  | 130.4     | 12.9  |
| 45.1  | 187.9     | 45.1  |
| 57.3  | 135.9     | 57.3  |
| 42.9  | 132.6     | 42.9  |
| 38.2  | 108.9 psi | 38.2  |
| 42.9  | 132.6     | 42.9  |
| 57.3  | 135.9     | 57.3  |
| 45.1  | 187.9     | 45.1  |
| 12.9  | 130.4     | 12.9  |
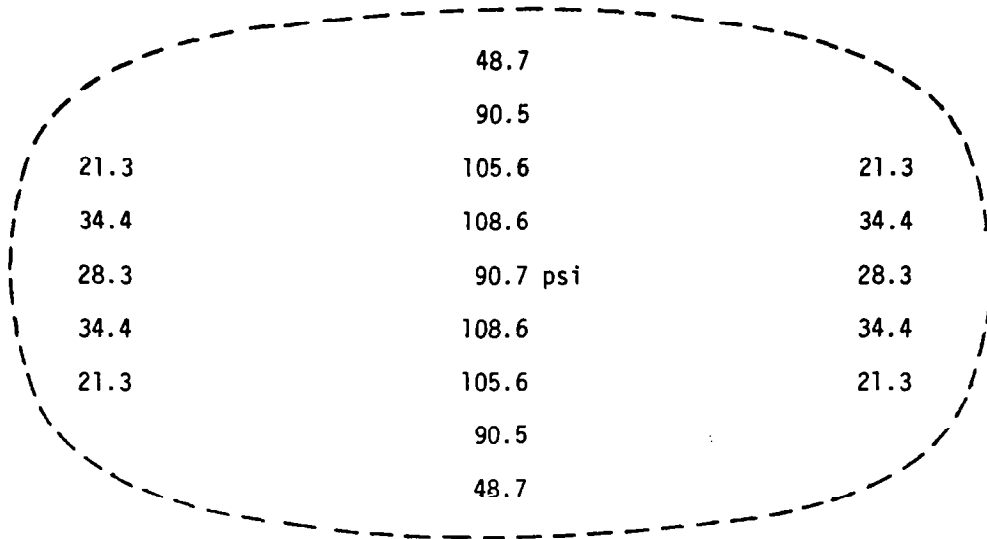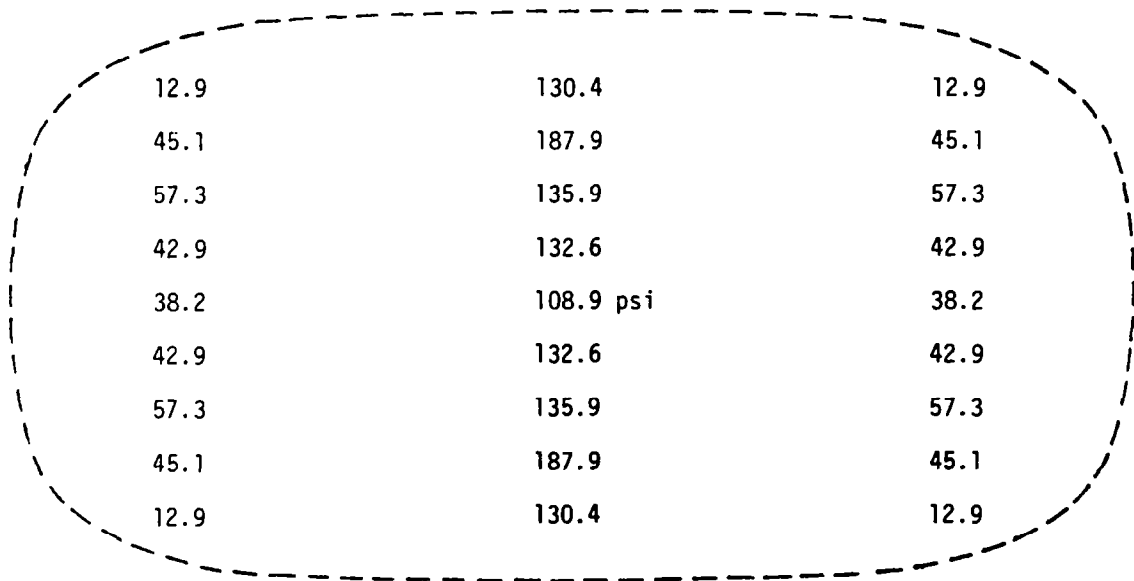
(b) δ = 1.00 in., Fz = 3700 lb

Figure 21

# EXTENSIONAL STRAINS DUE TO INFLATION PRESSURE

The extensional (membrane) strains produced by inflation pressure only are shown in figure 22. In this plot, $e_s$ is the strain in the direction of the meridian and $e_\theta$ is the strain in the circumferential direction. These strain distributions are axisymmetric and agree with the strains calculated by Brewer (ref. 5).
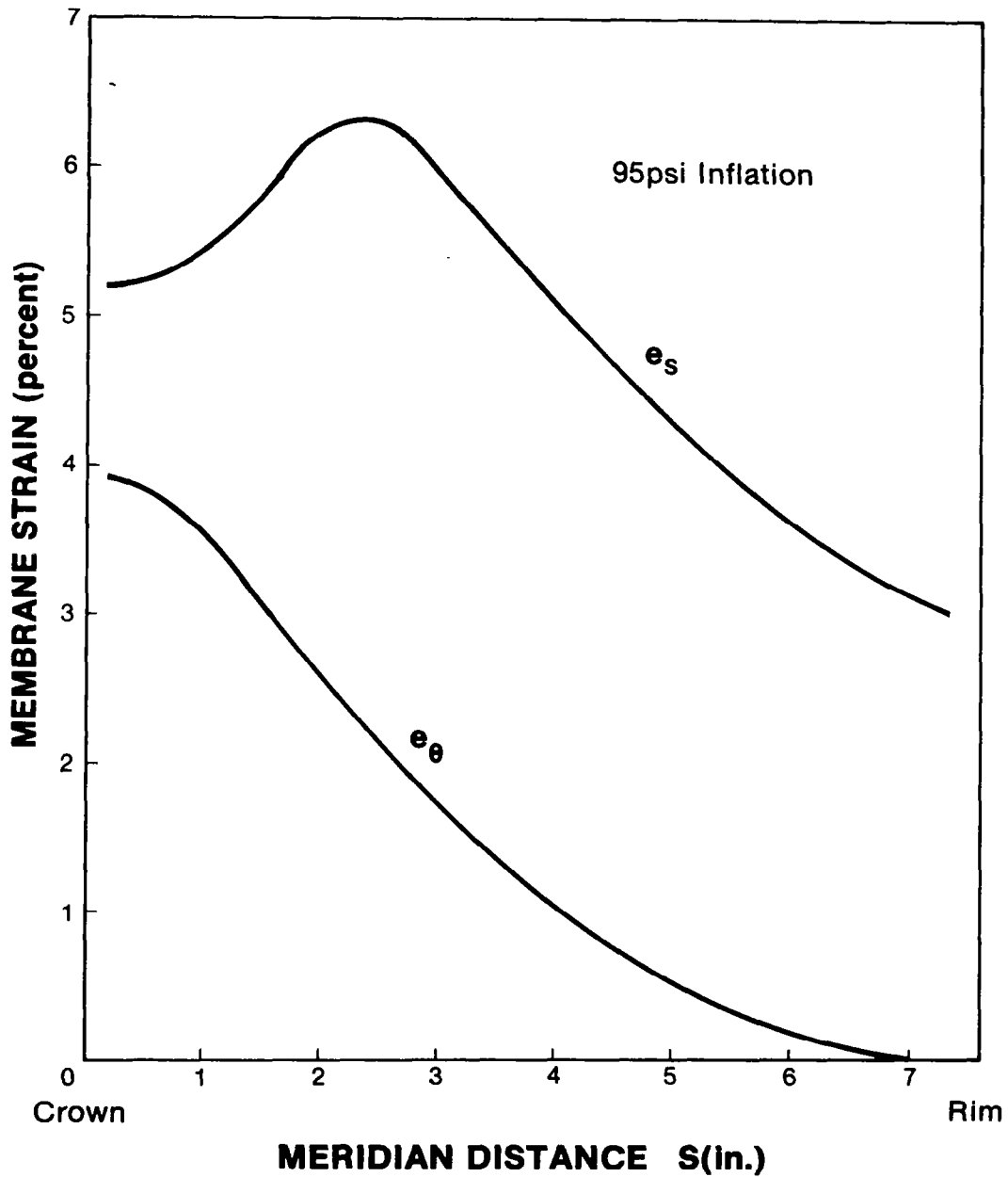


Figure 22

# FORCE RESULTANTS DUE TO INFLATION PRESSURE

The membrane forces (per unit length) produced by inflation pressure only are shown in figure 23. The forces $N_s$ and $N_\theta$ are in the meridional and circumferential directions, respectively. These force distributions are axisymmetric.
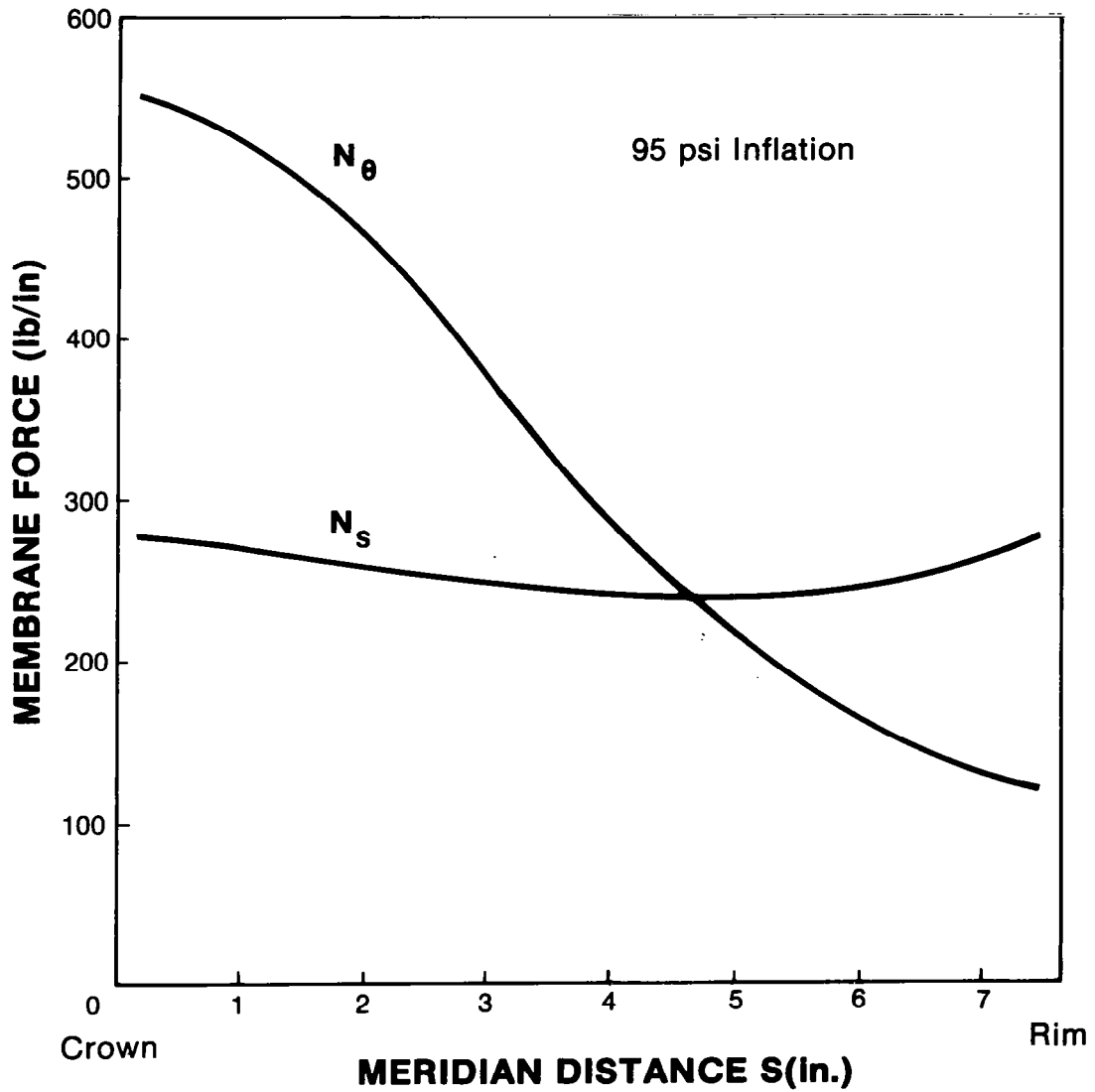


Figure 23

# REFERENCES

1. Tillerson, J. R.; and Haisler, W. E.: SAMMSOR II - A Finite Element Program to Determine Stiffness and Mass Matrices of Shells of Revolution. TEES-RPT-70-18, Texas A&M University, Oct. 1970.

2. Haisler, W. E.; and Stricklin, J. A.: SNASOR II - A Finite Element Program for the Static Nonlinear Analysis of Shells of Revolution. TEES-RPT-70-20, Texas A&M University, Oct. 1970.

3. Schapery, R. A.; and Tielking, J. T.: Investigation of Tire-Pavement Interaction During Maneuvering: Theory and Results. Report No. FHWA-RD-78-72, Federal Highway Administration, June 1977.

4. Tielking, J. T.; and Schapery, R. A.: A Method for Shell Contact Analysis. Computer Methods in Applied Mechanics and Engineering, Vol. 26, No. 2, pp. 181-195, May 1981.

5. Brewer, H. K.: Stresses and Deformations in Multi-Ply Aircraft Tires Subject to Inflation Pressure Loading. Report No. AFFDL-TR-70-62, Air Force Flight Dynamics Laboratory, June 1970.

6. Stafford, J. R.; and Tabaddor, F.: ADINA Load Updating for Pressurized Structures. Symposium on Finite Element Analysis of Tires, ASTM F-9, May 1980.